



Cite this: *CrystEngComm*, 2026, **28**, 577

## When halogen bonding isn't enough: solvation behavior in ionic cocrystals of benzyltrimethylammonium halides and 1,4-diodotetrafluorobenzene†

Andrew J. Peloquin, <sup>a</sup> Lahiruni Pelendage,<sup>a</sup> Srikar Alapati,<sup>b</sup> Timothy W. Hanks, <sup>b</sup> Colin D. McMillen \*<sup>a</sup> and William T. Pennington \*<sup>a</sup>

The role of halide anion identity and the influence of reaction solvent on the resulting halogen-bonded assembly was explored by combining 1,4-diodotetrafluorobenzene (*p*-F<sub>4</sub>DIB) with trimethylbenzyl ammonium halides (NMe<sub>3</sub>BzX, X = Cl, Br, I) in diverse organic solvents. Iodide salts predominantly yielded solvated crystalline products when the salt cocrystallized in an equimolar ratio with *p*-F<sub>4</sub>DIB. In solvent systems where the iodides did not crystallize as solvates, the salt:organoiodine ionic cocrystal ratio departed from the 1:1 reaction stoichiometry, producing 8:3, 4:5, or 2:3 cocrystals. In contrast, bromide and chloride analogues favored unsolvated forms, with chloride consistently producing a single 1:1 motif across multiple solvents. A small number of solvated forms were isolated in the Br and Cl series, typically at matched donor:acceptor ratios. Notably, chloride and bromide salts formed nearly indistinguishable halogen-bonded networks, apart from differences attributable to anion size. These results emphasize the delicate balance between solvent, stoichiometry, and halide identity in directing halogen-bond-driven crystallization.

Received 26th August 2025,  
Accepted 22nd November 2025

DOI: 10.1039/d5ce00832h

rsc.li/crystengcomm

## Introduction

Halogen bonding has become a central strategy in the design of supramolecular architectures, offering a directional, predictable, and highly tunable noncovalent interaction between a polarized halogen atom and an electron donor site.<sup>1,2</sup> This interaction, driven by the anisotropic distribution of electron density around halogen atoms, particularly iodine and bromine, has been widely exploited to construct cocrystals,<sup>3–5</sup> molecular assemblies,<sup>6–8</sup> and functional materials.<sup>9</sup> Halogen bonding complements and sometimes rivals hydrogen bonding in strength and selectivity, offering unique advantages in crystal engineering where geometrical precision is crucial.<sup>7,10,11</sup> Halogen bonding is an essential force in supramolecular chemistry,<sup>10,12,13</sup> liquid crystal formation,<sup>14–16</sup> and pharmaceutical development.<sup>17,18</sup>

Building on these advances, solvated halogen-bonded cocrystals—crystalline materials in which solvent molecules are incorporated into the lattice—present a compelling

subfield for exploration. Solvent molecules can participate directly in halogen bonding or indirectly modulate crystal packing *via* secondary interactions, such as hydrogen bonding, van der Waals forces, or  $\pi$ -stacking.<sup>19,20</sup> Their presence can stabilize otherwise inaccessible packing motifs,<sup>21–24</sup> resulting in diverse or tunable physical properties such as thermal behavior, mechanical integrity, and solubility.<sup>25,26</sup> For example, tetrahaloethynyl resorcinarene cavitands have been studied as solvates, where the structural flexibility of the cavitand was essential to the resulting solid-state structure. The authors noted “unpredictable intermolecular interactions where the fine balance between halogen and hydrogen bonding drives the crystallization process”.<sup>27</sup> Understanding the role of solvent inclusion is particularly relevant for pharmaceutical development, where control over solvate formation and desolvation profiles is crucial for manufacturability and regulatory compliance.<sup>28,29</sup> Despite their practical relevance, solvated halogen-bonded cocrystals remain relatively underexplored compared to their hydrogen-bonded counterparts, offering a fertile ground for expanding the toolkit of crystal design.

Herein, we report the isolation of twenty ionic cocrystals obtained by the reaction of the common halogen bond donor 1,4-diodotetrafluorobenzene (*p*-F<sub>4</sub>DIB) with the halide salts of the benzyltrimethylammonium cation (NMe<sub>3</sub>BzCl),

<sup>a</sup> Department of Chemistry, Clemson University, 219 Hunter Laboratories, Clemson, SC 29634-0973, USA. E-mail: cmcmill@clemson.edu, billp@clemson.edu

<sup>b</sup> Department of Chemistry, Furman University, Greenville, SC 29613, USA

† Dedicated to Professor Resnati, celebrating a career in fluorine and noncovalent chemistry on the occasion of his 70th birthday.



NMe<sub>3</sub>BzBr, and NMe<sub>3</sub>BzI) in a variety of solvents. *p*-F<sub>4</sub>DIB is a widely used, strong halogen bond donor due to its electron-withdrawing fluorine substituents, while quaternary ammonium halide salts offer flexible anionic templates, lacking significant directional or numeric limitations at the halide anion, making them suitable for exploring structure-directing effects in cocrystal formation.<sup>30–33</sup> The two-component system of (NMe<sub>3</sub>BzX):(p-F<sub>4</sub>DIB) can be equally interpreted as a three-component system of cation, anion, and organoiodine, or (NMe<sub>3</sub>Bz<sup>+</sup>)(X<sup>-</sup>):(p-F<sub>4</sub>DIB).

A search of the Cambridge Structural Database for cocrystals of *p*-F<sub>4</sub>DIB reveals 729 hits, with 105 of these containing at least one ionic component. Common ionic components include pyridine-*N*-oxides,<sup>34–36</sup> halides,<sup>37,38</sup> and various ammonium-containing cations.<sup>39–41</sup> Amongst the common organic solvents, solvates with methanol,<sup>37,38</sup> ethanol,<sup>38</sup> dichloromethane,<sup>42,43</sup> chloroform,<sup>38</sup> acetone,<sup>44</sup> acetonitrile,<sup>44–47</sup> toluene<sup>48</sup> have been previously reported. For the salts NMe<sub>3</sub>BzCl and NMe<sub>3</sub>BzBr, unsolvated ionic cocrystals were more likely to be isolated, whereas the iodide salt provided primarily solvated ionic cocrystals of varying stoichiometry. The bromide and chloride-containing ionic cocrystals were often isostructural. Trends in void volume were analyzed using CCDC's *Mercury*<sup>49</sup> as well as the IUCr's *checkCIF*,<sup>50–52</sup> revealing a significant chasm in the void volumes between the solvated and unsolvated structures.

## Experimental

### Synthesis of ionic cocrystals

Benzyltrimethylammonium chloride (purity 97%, CAS registry number 56-93-9), benzyltrimethylammonium bromide (purity 95+%, CAS registry number 5350-41-4), and 1,4-diiodotetrafluorobenzene (purity 97%, CAS registry number 392-57-4) were obtained from Oakwood Chemical. Benzyltrimethylammonium iodide (purity 95%, CAS registry number 4525-46-6) was obtained from Millipore Sigma. All

reagents and solvents were used as received. All ionic cocrystals were obtained *via* a 1:1 molar ratio reaction of the benzyltrimethylammonium halide salt and 1,4-diiodotetrafluorobenzene in the respective solvent under ambient conditions (Table 1). Many of the solvates had limited stability outside of the mother liquor, so no thermal analysis or powder X-ray diffraction studies were conducted. A representative synthesis is included.

**Synthesis of NMe<sub>3</sub>BzI:p-F<sub>4</sub>DIB:EtOH.** As a representative synthesis, benzyltrimethylammonium iodide (41 mg, 0.15 mmol) and 1,4-diiodotetrafluorobenzene (59 mg, 0.15 mmol) were combined with vigorous stirring in ca 10 mL of ethanol. Once dissolved, stirring was stopped, and the solvent was allowed to evaporate slowly under ambient conditions. Once crystal growth was observed, the vial was sealed to limit potential solvent loss or crystal decomposition. In most solvent systems, cocrystal formation was observed within seven days. Most of the solvated ionic cocrystals exhibited very limited stability outside of their mother liquor. Complete synthetic details for all twenty ionic cocrystals are provided in the SI.

**X-ray crystallography.** For single-crystal X-ray analysis, crystals were mounted on low-background cryogenic loops using paratone oil. Data were collected using Mo K $\alpha$  radiation ( $\lambda = 0.71073$  Å) on a Bruker D8 Venture diffractometer with an Incoatec Iμs microfocus source and a Photon 2 detector or a Bruker D8 Quest diffractometer with a Photon 100 detector. Diffraction data were collected using  $\varphi$  and  $\omega$ -scans and subsequently processed (SAINT) and scaled (SADABS) using the APEX3 software suite.<sup>53</sup> The structures were solved by intrinsic phasing (SHELXT) and refined by full-matrix least-squares techniques (SHELXL) on  $F^2$  using the SHELXTL software suite.<sup>54,55</sup>

All non-hydrogen atoms were refined anisotropically. As the acetonitrile molecules in 2(NMe<sub>3</sub>BzCl):2(*p*-F<sub>4</sub>DIB):MeCN, 2(NMe<sub>3</sub>BzBr):2(*p*-F<sub>4</sub>DIB):MeCN, and 4(NMe<sub>3</sub>BzI):4(*p*-F<sub>4</sub>DIB):MeCN lie on symmetry elements, they were constrained with a combination of DFIX, DANG, ISOR, and SIMU to achieve

**Table 1** Ionic cocrystals obtained by NMe<sub>3</sub>BzX salt and solvent

Solvent	NMe <sub>3</sub> BzX salt		
	NMe <sub>3</sub> BzCl	NMe <sub>3</sub> BzBr	NMe <sub>3</sub> BzI
Methanol (MeOH)	NMe <sub>3</sub> BzCl: <i>p</i> -F <sub>4</sub> DIB	NMe <sub>3</sub> BzBr: <i>p</i> -F <sub>4</sub> DIB	NMe <sub>3</sub> BzI: <i>p</i> -F <sub>4</sub> DIB:MeOH
Ethanol (EtOH)	NMe <sub>3</sub> BzCl: <i>p</i> -F <sub>4</sub> DIB	3(NMe <sub>3</sub> BzBr):4( <i>p</i> -F <sub>4</sub> DIB)	2(NMe <sub>3</sub> BzI):3( <i>p</i> -F <sub>4</sub> DIB)
<i>iso</i> -Propanol ( <i>i</i> -PrOH)	NMe <sub>3</sub> BzCl: <i>p</i> -F <sub>4</sub> DIB	3(NMe <sub>3</sub> BzBr):4( <i>p</i> -F <sub>4</sub> DIB)	NMe <sub>3</sub> BzI: <i>p</i> -F <sub>4</sub> DIB:EtOH
<i>Tert</i> -Butanol ( <i>t</i> -BuOH)	NMe <sub>3</sub> BzCl: <i>p</i> -F <sub>4</sub> DIB	3(NMe <sub>3</sub> BzBr):4( <i>p</i> -F <sub>4</sub> DIB)	NMe <sub>3</sub> BzI: <i>p</i> -F <sub>4</sub> DIB: <i>i</i> -PrOH
Acetonitrile (MeCN)	2(NMe <sub>3</sub> BzCl):2( <i>p</i> -F <sub>4</sub> DIB):MeCN	2(NMe <sub>3</sub> BzBr):2( <i>p</i> -F <sub>4</sub> DIB):MeCN	4(NMe <sub>3</sub> BzI):5( <i>p</i> -F <sub>4</sub> DIB)
Acetone (Ace)	NMe <sub>3</sub> BzCl: <i>p</i> -F <sub>4</sub> DIB:Ace	NMe <sub>3</sub> BzBr: <i>p</i> -F <sub>4</sub> DIB:Ace	4(NMe <sub>3</sub> BzI):4( <i>p</i> -F <sub>4</sub> DIB):MeCN
Dichloromethane (DCM)	NMe <sub>3</sub> BzCl: <i>p</i> -F <sub>4</sub> DIB	4(NMe <sub>3</sub> BzBr):5( <i>p</i> -F <sub>4</sub> DIB)	4(NMe <sub>3</sub> BzI):4( <i>p</i> -F <sub>4</sub> DIB):3(Ace)
Chloroform (CHCl <sub>3</sub> )	3(NMe <sub>3</sub> BzCl):3( <i>p</i> -F <sub>4</sub> DIB):2(CHCl <sub>3</sub> )	<sup>a</sup>	2(NMe <sub>3</sub> BzI):2( <i>p</i> -F <sub>4</sub> DIB):2(DCM)
Iodomethane (CH <sub>3</sub> I)	2(NMe <sub>3</sub> BzI):2( <i>p</i> -F <sub>4</sub> DIB):CH <sub>3</sub> I <sup>b</sup>	2(NMe <sub>3</sub> BzI):2( <i>p</i> -F <sub>4</sub> DIB):CH <sub>3</sub> I <sup>b</sup>	2(NMe <sub>3</sub> BzI):2( <i>p</i> -F <sub>4</sub> DIB):CHCl <sub>3</sub>
Toluene	<sup>c</sup>	<sup>c</sup>	8(NMe <sub>3</sub> BzI):3( <i>p</i> -F <sub>4</sub> DIB)
Ethylene glycol	NMe <sub>3</sub> BzCl: <i>p</i> -F <sub>4</sub> DIB		4(NMe <sub>3</sub> BzI):5( <i>p</i> -F <sub>4</sub> DIB)

<sup>a</sup> The crystal structure of the resulting crystals could not be reliably determined due to extensive twinning. <sup>b</sup> We note that *in situ* decomposition of the CH<sub>3</sub>I solvent led to the formation of the solvated iodide salt cocrystal in all cases. <sup>c</sup> We observed recrystallization of the starting materials rather than formation of a cocrystal.



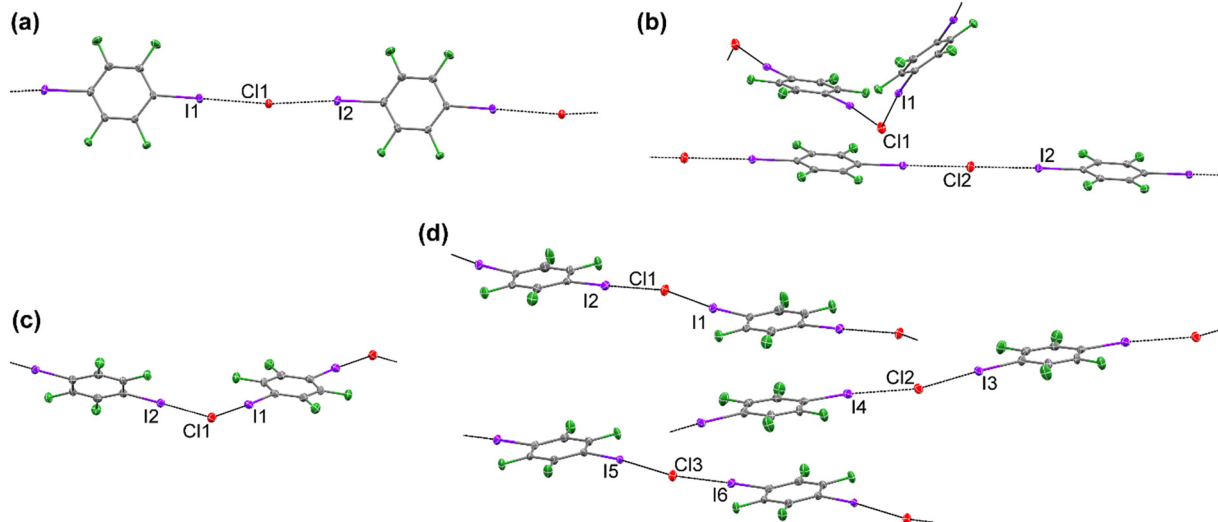


**Fig. 1** Halogen bonding in  $\text{NMe}_3\text{BzCl}:p\text{-F}_4\text{DIB}$  (a) (viewed down the  $c$  axis),  $2(\text{NMe}_3\text{BzCl}):2(p\text{-F}_4\text{DIB})\text{:MeCN}$  (b) (viewed down the  $c^*$  axis),  $\text{NMe}_3\text{BzCl}:p\text{-F}_4\text{DIB}\text{:Ace}$  (c) (viewed down the  $b$  axis), and  $3(\text{NMe}_3\text{BzCl}):3(p\text{-F}_4\text{DIB})\text{:2(CHCl}_3$  (d). Solvent molecules and hydrogen atoms are omitted for clarity. Atomic displacement ellipsoids are displayed at the 50% probability level. Carbon atoms are gray, fluorine atoms green, iodine atoms purple, chlorine atoms red, and bromine atoms brown.

chemically reasonable geometries. Two orientations of the ethanol molecule in  $\text{NMe}_3\text{BzI}:p\text{-F}_4\text{DIB}\text{:EtOH}$  were modeled with reasonable SIMU constraints. Disorder within the acetone molecules of  $4(\text{NMe}_3\text{BzI}):4(p\text{-F}_4\text{DIB})\text{:3(Ace)}$  was constrained using reasonable SIMU constraints. The SI (Table SI1) provides crystallographic data from the structure refinements.

### Void calculations-methods

Solvent accessible void volumes were calculated using the crystal structure visualization and analysis software Mercury, designed by the Cambridge Crystallographic Data Centre (CCDC).<sup>49</sup> The pore analyzer tool was utilized to calculate the volumes of the void spaces with the solvents manually

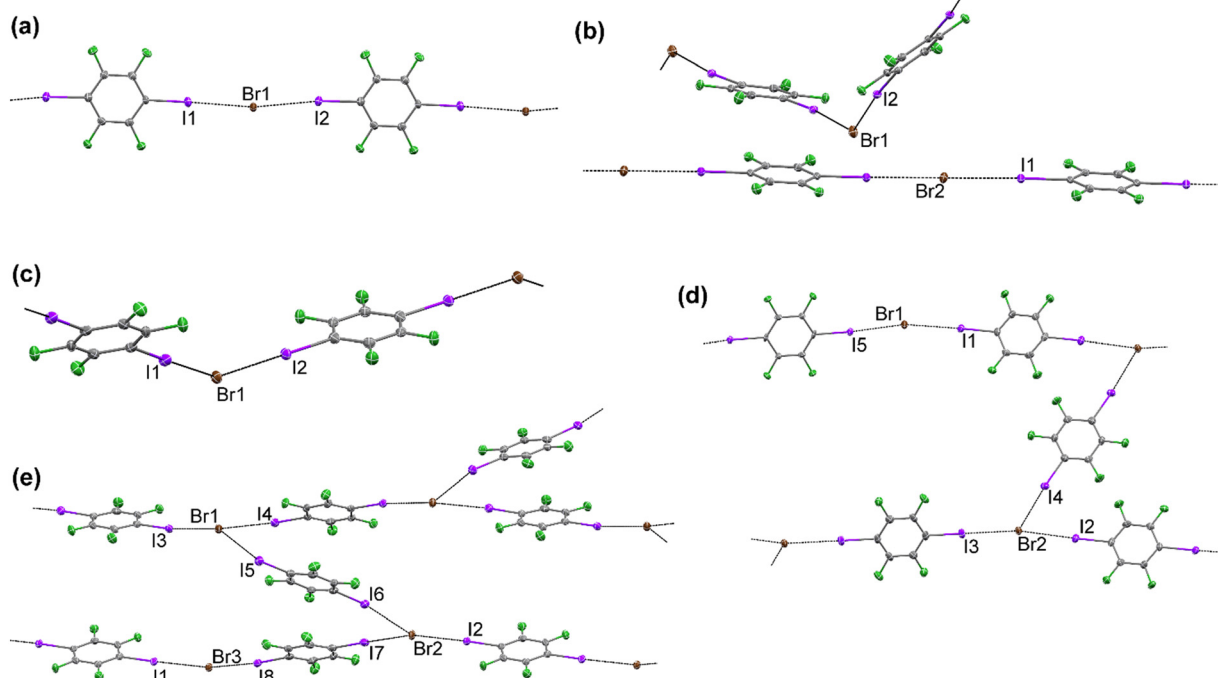


**Fig. 2** Halogen bonding in  $\text{NMe}_3\text{BzBr}:p\text{-F}_4\text{DIB}$  (a),  $2(\text{NMe}_3\text{BzBr}):2(p\text{-F}_4\text{DIB})\text{:MeCN}$  (b),  $\text{NMe}_3\text{BzBr}:p\text{-F}_4\text{DIB}\text{:Ace}$  (c),  $4(\text{NMe}_3\text{BzBr}):5(p\text{-F}_4\text{DIB})$  (d), and  $3(\text{NMe}_3\text{BzBr}):4(p\text{-F}_4\text{DIB})$  (e). Solvent molecules and hydrogen atoms are omitted for clarity. Atomic displacement ellipsoids are displayed at the 50% probability level.

removed through the software. This gave an assortment of data about the properties of these void spaces. Accessible helium volume showed the volume that a single helium atom (van der Waals volume of  $0.2073 \text{ \AA}^3$ ) can access in the given void space, and maximum pore diameter showed the diameter of the largest sphere in the given void space. Visualization of these spaces without solvent molecules were done through the “Display Voids” feature which allows the user to set the spherical probe size. We chose the size of  $1.2 \text{ \AA}$  as this is the size of the average water molecule with grid spacing of  $0.2 \text{ \AA}$ . The grid space refers to the resolution of the 3D grid used to probe the crystal structure. This means that lower grid spacing leads to a higher resolution and more accurate calculation of the void space.

The Kitaigorodskii Packing Index (KPI) was calculated using the software PLATON.<sup>51,52,56</sup> KPI refers to how tight molecules are packed in the crystal structure, with lower values indicating less packed and more space for solvent accessible voids. Using the “CALC VOID” method, the van der Waals sphere around each atom is calculated and is compared to the total unit cell volume. This results in the KPI, total volume taken up by all the molecules, total unit cell volume, and a percentage of the void spaces based on the previous two volumes. Default probe size and grid spacing are  $1.2 \text{ \AA}$  and  $0.2 \text{ \AA}$  as done in calculating void spaces using Mercury; however, values may not be an exact match as each software processes these void spaces differently. We chose to use the void space volume from Mercury and the KPI from PLATON when comparing each crystal.

## Results and discussion

### Unsolvated ionic cocrystals

The majority of solvents with the chloride and bromide salts,  $\text{NMe}_3\text{BzCl}$  and  $\text{NMe}_3\text{BzBr}$ , provided unsolvated ionic cocrystals. In the simplest cases, the overall structural motifs are quite similar in the two 1:1 ionic cocrystals  $\text{NMe}_3\text{BzCl}:p\text{-F}_4\text{DIB}$  and  $\text{NMe}_3\text{BzBr}:p\text{-F}_4\text{DIB}$ . Both of these crystallize in the space group  $Cc$ , with an expected small expansion of unit cell dimensions ( $0.1\text{--}0.5 \text{ \AA}$ ) to accommodate the larger bromide anion. Halogen bonding directs the formation of 1-dimensional chains, consisting of halogen anions and  $p\text{-F}_4\text{DIB}$  molecules, alternating in the  $[1 \ 1 \ 0]$  and  $[-1 \ 1 \ 0]$  directions (Fig. 1a and 2a). The halogen bonding interactions in both ionic cocrystals are nearly linear, with  $\text{C}-\text{I}\cdots\text{A}$  ( $\text{A} = \text{Cl}^-, \text{Br}^-$ ) ranging from  $173.87(7)^\circ$  to  $178.44(4)^\circ$ , with slight expansion of the halogen bonding distance from  $3.1271(5) \text{ \AA}$  and  $3.1071(5) \text{ \AA}$  with chloride to  $3.2434(3) \text{ \AA}$  and  $3.2332(4) \text{ \AA}$  with bromide. Adjusting for the increased ionic radii of bromide *versus* chloride, the  $R_{\text{XB}}$  values<sup>57,58</sup> (that is, the halogen bond lengths, normalized to the sum of the van der Waals radii) are consistent between the two ionic cocrystals, all falling within the range of 0.83 to 0.85.

Two additional ionic cocrystal ratios were accessible from reactions with the bromide salt. While the 1:1 ionic cocrystal was obtained from methanol, the  $3(\text{NMe}_3\text{BzBr}):4(p\text{-F}_4\text{DIB})$

ionic cocrystal was obtained from ethanol, *iso*-propanol, and *tert*-butanol (Fig. 2e). This contrasts with the chloride salt, from which the 1:1 ionic cocrystal was obtained from all four alcohols studied. In  $3(\text{NMe}_3\text{BzBr}):4(p\text{-F}_4\text{DIB})$ , slightly kinked chains, with  $\text{I}\cdots\text{Br}\cdots\text{I}$  angles between  $162.461(14)^\circ$  and  $167.128(11)^\circ$ , are interconnected by another  $p\text{-F}_4\text{DIB}$  molecule, with the acute  $\text{I}\cdots\text{Br}\cdots\text{I}$  angles measuring  $72.943(11)^\circ$  and  $71.364(10)^\circ$ . This combination of halogen bonding interactions results in the formation of folded ribbons. From dichloromethane as the crystallization solvent,  $4(\text{NMe}_3\text{BzBr}):5(p\text{-F}_4\text{DIB})$  was obtained (Fig. 2d). Similar to the 3:4 ionic cocrystal, slightly kinked chains are present within the 4:5 ionic cocrystal, with  $\text{I}\cdots\text{Br}\cdots\text{I}$  angles of  $162.55(3)^\circ$  and  $165.68(3)^\circ$ . The chains are also linked through halogen bonding by another  $p\text{-F}_4\text{DIB}$  molecule, with an acute angle of  $73.78(2)^\circ$ . The change in crystallographic symmetry from  $Pna2_1$  in the 3:4 ionic cocrystal to  $P2_1/c$  in the 4:5 ionic cocrystal facilitates a significant difference in the overall halogen bonding motif. In both systems, the chains of

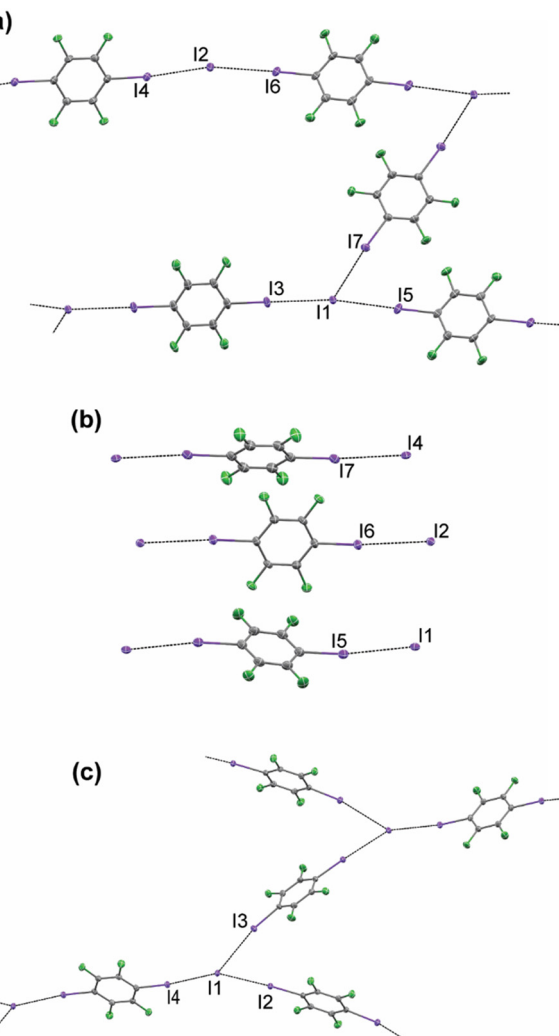


Fig. 3 Halogen bonding in  $4(\text{NMe}_3\text{BzI}):5(p\text{-F}_4\text{DIB})$  (a),  $8(\text{NMe}_3\text{BzI}):3(p\text{-F}_4\text{DIB})$  (b), and  $2(\text{NMe}_3\text{BzI}):3(p\text{-F}_4\text{DIB})$  (c).



alternating layers propagate in  $[0\ 1\ 1]$  and  $[0\ 1\ -1]$  directions. The combination of halogen bonding interactions in the 4:5 ionic cocrystal results in the formation of interpenetrating sheets, with a plane-to-plane angle of approximately  $49^\circ$ .

While the majority of solvents provided solvated ionic cocrystals when using  $\text{NMe}_3\text{BzI}$ , three unsolvated motifs were obtained: 4( $\text{NMe}_3\text{BzI}$ ):5( $p\text{-F}_4\text{DIB}$ ), 8( $\text{NMe}_3\text{BzI}$ ):3( $p\text{-F}_4\text{DIB}$ ), and 2( $\text{NMe}_3\text{BzI}$ ):3( $p\text{-F}_4\text{DIB}$ ) (Fig. 3). The 4:5 ionic cocrystal is obtained when using ethylene glycol as the reaction solvent in the space group  $P2_1/c$ , just as in the 4( $\text{NMe}_3\text{BzBr}$ ):5( $p\text{-F}_4\text{DIB}$ ) system. Once again, chains are interconnected by  $p\text{-F}_4\text{DIB}$  molecules to form sheets. These interpenetrating sheets intersect at approximately  $49^\circ$ , matching the packing within the 4( $\text{NMe}_3\text{BzBr}$ ):5( $p\text{-F}_4\text{DIB}$ ) system. The 8( $\text{NMe}_3\text{BzI}$ ):3( $p\text{-F}_4\text{DIB}$ ) system crystallizes in the space group  $P\bar{1}$  from toluene. In this case, in contrast to the extended halogen bonding motifs seen in the previously described systems, this ionic cocrystal contains three distinct, isolated halogen bonding units each consisting of one  $p\text{-F}_4\text{DIB}$  molecule “capped” by two iodide anions through C–F···I halogen bonding. The remaining two iodide anions fill space within

the crystal lattice but are not involved in significant halogen bonding interactions. This is the only example in this study where long-range halogen bonding patterns were not observed. The final unsolvated, iodide-containing ionic cocrystal, 2( $\text{NMe}_3\text{BzI}$ ):3( $p\text{-F}_4\text{DIB}$ ), was obtained from the same reaction that produced  $\text{NMe}_3\text{BzI}$ : $p\text{-F}_4\text{DIB}$ :MeOH. The halogen bonding motif is similar to that of 4( $\text{NMe}_3\text{BzBr}$ ):5( $p\text{-F}_4\text{DIB}$ ), with chains consisting of alternating  $p\text{-F}_4\text{DIB}$  molecules and iodide anions, kinked at  $45.228(6)^\circ$  and  $35.548(6)^\circ$  about the two unique C–I···I–C halogen bonds. The chains are linked into sheets *via* a  $p\text{-F}_4\text{DIB}$  molecule, with an acute angle of  $70.045(5)^\circ$  at the junction.

### Solvated ionic cocrystals

When utilizing the chloride and bromide salts, acetonitrile, acetone, and chloroform yielded solvated ionic cocrystals. Both the chloride and bromide-containing cocrystals, 2( $\text{NMe}_3\text{BzCl}$ ):2( $p\text{-F}_4\text{DIB}$ ):MeCN and 2( $\text{NMe}_3\text{BzBr}$ ):2( $p\text{-F}_4\text{DIB}$ ):MeCN respectively (Fig. 1b and 2b), crystallize in the space group  $C2/c$ , with one fully unique  $\text{NMe}_3\text{Bz}^+$  cation, two half

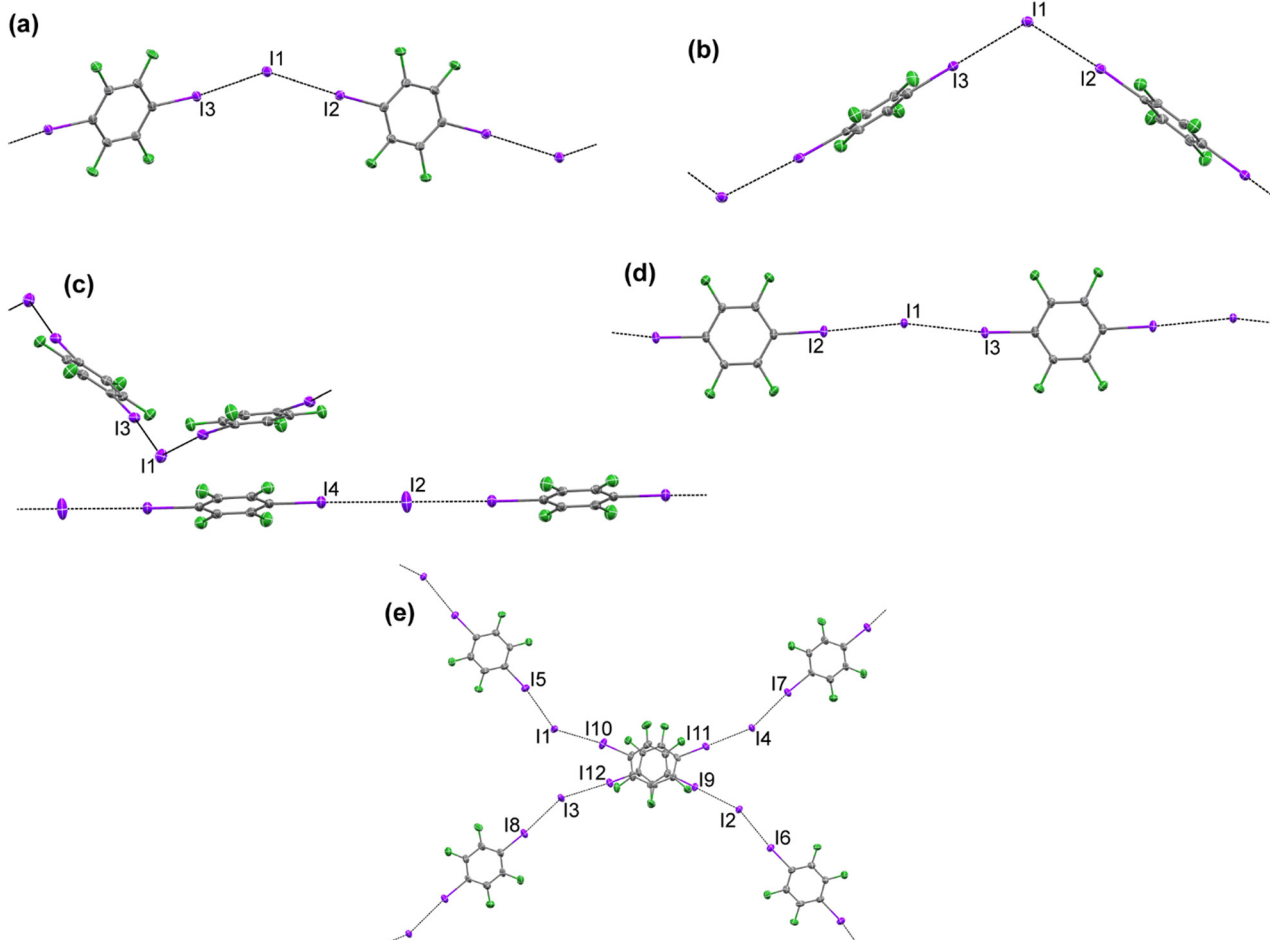


Fig. 4 Halogen bonding in  $\text{NMe}_3\text{BzI}$ : $p\text{-F}_4\text{DIB}$ : $i\text{-PrOH}$  (a),  $\text{NMe}_3\text{BzI}$ : $p\text{-F}_4\text{DIB}$ :MeOH (b), 4( $\text{NMe}_3\text{BzI}$ ):4( $p\text{-F}_4\text{DIB}$ ):MeCN (c), 2( $\text{NMe}_3\text{BzI}$ ):2( $p\text{-F}_4\text{DIB}$ ): $\text{CH}_3\text{I}$  (d), 4( $\text{NMe}_3\text{BzI}$ ):4( $p\text{-F}_4\text{DIB}$ ):3(Ac) (e). Solvent molecules and hydrogen atoms are omitted for clarity. Atomic displacement ellipsoids are displayed at the 50% probability level.



unique halide anions, two half unique *p*-F<sub>4</sub>DIB molecules, and one half occupied solvent molecule within the asymmetric unit. Two distinct halogen bonding motifs are observed. Kinked 1:1 chains consisting of alternating halogen anions and *p*-F<sub>4</sub>DIB molecules propagate in the *c* direction and lie within the (0 1 1) plane, with I···X···I angles of 127.85(5)° and 132.255(15)° in the chloride and bromide ionic cocrystals, respectively. The second motif is that of a linear chain propagating in the [1 1 0] direction. The acetonitrile molecule is disordered over an inversion center, and therefore the occupancy of the two positions is one-half each. The ionic cocrystal obtained from acetonitrile and NMe<sub>3</sub>BzI also crystallizes in the *C*2/*c* space group. (Fig. 4c) In this case, the asymmetric unit contains a solvent molecule disordered over an inversion center, with an occupancy of the two positions one-fourth each, resulting in a 4:4:1 ratio. Despite the change in the overall stoichiometric ratio, the halogen bonding pattern remains consistent, consisting of both kinked and straight chains. In this case, however, the chains are oriented differently relative to the unit cell directions. The kinked chains propagate in the [1 0 1] direction and lie within the (1 0 1) plane. The I···I···I angle of 137.493(12)° establishes the trend of increasing angle moving from chloride to bromide to iodide. The straight chains align in the [1 1 0] direction.

Utilizing acetone as the crystallization solvent provides another opportunity to compare the solvated structures of all three halide salts. The chloride-containing structure NMe<sub>3</sub>BzCl:*p*-F<sub>4</sub>DIB:Ace is obtained in the space group *P*2<sub>1</sub>/*n*, and the corresponding bromide-containing structure NMe<sub>3</sub>BzBr:*p*-F<sub>4</sub>DIB:Ace is obtained in *P*2<sub>1</sub>/*c*, although both have similar reduced cells indicative of isomorphous structures. In both

structures, the asymmetric unit consists of an NMe<sub>3</sub>BzX ion pair, an acetone solvent molecule, and two unique half-molecules of *p*-F<sub>4</sub>DIB. In both structures, the primary halogen bonding motif is that of slightly kinked chains of alternating *p*-F<sub>4</sub>DIB molecules and halide ions (I···X···I of 148.99(3)° and 147.913(11)° in the chloride and bromide structures, respectively) aligned in the *bc* plane. Moving along the *a* axis, chains stack orthogonally to one another (*i.e.* chains in one plane propagate in the [0 1 1] direction, with chains in the next plane in the [0 -1 1] direction). Just as with the acetonitrile solvate series, the acetone solvate of the iodide salt, 4(NMe<sub>3</sub>BzI):4(*p*-F<sub>4</sub>DIB):3(Ace), is obtained in a different ratio, although in the lower symmetry *P*2<sub>1</sub> space group (Fig. 4e). Once again, the primary halogen bonding motif is that of kinked chains, with I···I···I angles ranging from 136.796(12)° to 156.650(12)°. In this case, chains propagating in structures, the asymmetric unit consists of an NMe<sub>3</sub>BzX ion pair, an acetone solvent molecule, and two unique half-molecules of *p*-F<sub>4</sub>DIB. In both structures, the primary halogen bonding motif is that of slightly kinked chains of alternating *p*-F<sub>4</sub>DIB molecules and halide ions (I···X···I of 148.99(3)° and 147.913(11)° in the chloride and bromide structures, respectively) aligned in the *bc* plane. Moving along the *a* axis, chains stack orthogonally to one another (*i.e.* chains in one plane propagate in the [0 1 1] direction, with chains in the next plane in the [0 -1 1] direction). Just as with the acetonitrile solvate series, the acetone solvate of the iodide salt, 4(NMe<sub>3</sub>BzI):4(*p*-F<sub>4</sub>DIB):3(Ace), is obtained in a different ratio, although in the lower symmetry *P*2<sub>1</sub> space group (Fig. 4e). Once again, the primary halogen bonding motif is that of kinked chains, with I···I···I angles ranging from 136.796(12)° to 156.650(12)°. In this case, chains propagating

**Table 2** Solvent accessible void volumes as calculated within *Mercury*, *IUCr checkCIF*, and *PLATON*

	Accessible helium volume (Å <sup>3</sup> )	Maximum pore diameter (Å)	Solvent accessible void (Å <sup>3</sup> )	KPI (%)	KPI w/ solvent removed (%)
2(NMe <sub>3</sub> BzI):3( <i>p</i> -F <sub>4</sub> DIB)	124.212	1.90		<sup>a</sup>	
8(NMe <sub>3</sub> BzI):3( <i>p</i> -F <sub>4</sub> DIB)	77.146	2.21		65.7	
3(NMe <sub>3</sub> BzBr):4( <i>p</i> -F <sub>4</sub> DIB)	211.567	2.37		67.3	
NMe <sub>3</sub> BzCl: <i>p</i> -F <sub>4</sub> DIB	109.095	2.61		63.1	
NMe <sub>3</sub> BzBr: <i>p</i> -F <sub>4</sub> DIB	132.77	2.62		62.4	
4(NMe <sub>3</sub> BzBr):5( <i>p</i> -F <sub>4</sub> DIB)	180.512	2.66		66.0	
4(NMe <sub>3</sub> BzI):5( <i>p</i> -F <sub>4</sub> DIB)	247.29	2.67		64.5	
4(NMe <sub>3</sub> BzI):4( <i>p</i> -F <sub>4</sub> DIB):MeCN	628.497	3.61	103	<sup>a</sup>	62.6
2(NMe <sub>3</sub> BzBr):2( <i>p</i> -F <sub>4</sub> DIB):MeCN	480.534	3.69	87	70.0	64.6
2(NMe <sub>3</sub> BzI):2( <i>p</i> -F <sub>4</sub> DIB):DCM	621.513	3.73	108	67.3	62.2
2(NMe <sub>3</sub> BzCl):2( <i>p</i> -F <sub>4</sub> DIB):MeCN	438.92	3.85	82	71.1	65.6
NMe <sub>3</sub> BzCl: <i>p</i> -F <sub>4</sub> DIB:Ace	505.477	4.03	112	67.8	57.1
NMe <sub>3</sub> BzI: <i>p</i> -F <sub>4</sub> DIB:MeOH	772.596	4.07	159	66.7	60.6
NMe <sub>3</sub> BzBr: <i>p</i> -F <sub>4</sub> DIB:Ace	532.089	4.11	121	<sup>a</sup>	56.0
2(Me <sub>3</sub> BzI):2( <i>p</i> -F <sub>4</sub> DIB):CH <sub>3</sub> I	430.927	4.12	112	66.0	61.3
2(NMe <sub>3</sub> BzI):2( <i>p</i> -F <sub>4</sub> DIB):CHCl <sub>3</sub>	756.621	4.49	154	66.6	60.4
NMe <sub>3</sub> BzI: <i>p</i> -F <sub>4</sub> DIB:EtOH	932.854	4.5	190	67.7	59.0
NMe <sub>3</sub> BzI: <i>p</i> -F <sub>4</sub> DIB: <i>i</i> -PrOH	292.257	4.62	236	67.6	56.6
3(NMe <sub>3</sub> BzCl):3( <i>p</i> -F <sub>4</sub> DIB):2(CHCl <sub>3</sub> )	773.939	4.7	156	66.0	61.6
4(NMe <sub>3</sub> BzI):4( <i>p</i> -F <sub>4</sub> DIB):3(Ace)	1005.59	5.3	<sup>b</sup>	65.2	57.5

For KPI, the full structure was analysed, including any solvent molecules. All other data was calculated after manually removing the solvent molecules. <sup>a</sup> No solvent accessible void was reported by *PLATON*, or KPI was not able to be calculated due to solvent disorder. <sup>b</sup> Solvent accessible void was reported by *checkCIF* as too large for detailed analysis.



in the same direction align in the *ac* plane, with the propagation direction varying for successive chains in different layers along the *b* axis.

When iodomethane was utilized as the crystallization solvent,  $2(\text{NMe}_3\text{BzI}):2(p\text{-F}_4\text{DIB}):CH_3\text{I}$  was obtained regardless of which halide salt was used in the reaction (Fig. 4d). This is likely due to the formation of iodide anions during the decomposition of iodomethane, resulting in the preferential crystallization of iodide salts over their chloride or bromide analogs. The primary  $\text{C}\cdots\text{I}\cdots\text{I}\cdots\text{C}$  halogen bonding forms kinked chains ( $\text{I}\cdots\text{I}\cdots\text{I}$  of  $166.710(7)^\circ$ ). Chain propagation direction varies while moving along the *c* axis, from  $[1\ 0\ 0]$  to  $[1\ 1\ 0]$  to  $[0\ 1\ 0]$ .

The remaining solvated ionic cocrystals were obtained only in the  $\text{NMe}_3\text{BzI}:p\text{-F}_4\text{DIB}$  system. These occurred in reactions with methanol, ethanol, isopropanol, dichloromethane, and chloroform. In the chloride and bromide systems, the alcohols and dichloromethane yielded only non-solvated ionic cocrystals. Chloroform yielded a  $3:3:2$  solvated ionic cocrystal when utilizing the chloride salt, differing from the  $2:2:1$  ratio of the iodide salt. The packing in the  $\text{NMe}_3\text{BzI}:p\text{-F}_4\text{DIB}:\text{MeOH}$  (Fig. 4b) and  $\text{NMe}_3\text{BzI}:p\text{-F}_4\text{DIB}:\text{EtOH}$  ionic cocrystals is quite similar, with only slight expansions in the orthorhombic cell parameters. In contrast, the  $\text{NMe}_3\text{BzI}:p\text{-F}_4\text{DIB}:i\text{-PrOH}$  (Fig. 4a) ionic cocrystals are obtained in the space group  $P\bar{1}$ . Halogen bonding drives the formation of kinked chains in all three systems. The  $\text{C}\cdots\text{I}\cdots\text{I}\cdots\text{C}$  angle in the methanol and ethanol systems is similar,  $109.466(18)^\circ$  and  $112.58(1)^\circ$ , respectively, whereas the chains in the *i*-PrOH system show less bending at  $146.199(6)^\circ$ . The  $2(\text{NMe}_3\text{BzI}):2(p\text{-F}_4\text{DIB}):DCM$  ionic cocrystal obtained from dichloromethane shows a halogen bonding motif similar to the iodide-containing acetonitrile solvated ionic cocrystal (Fig. 4c), with both straight and kinked chain. The  $\text{C}\cdots\text{I}\cdots\text{I}\cdots\text{C}$  angle of  $136.554(14)^\circ$  is also similar to the acetonitrile system. Finally, the halogen bonding observed in the chloroform solvate  $2(\text{NMe}_3\text{BzI}):2(p\text{-F}_4\text{DIB}):CHCl_3$  is analogous to that of the acetone-containing system (Fig. 4e), with chains in the *ac* plane alternating their propagation direction as they stack in the *b* direction.

### Pore diameter comparison

An analysis of pore diameter, as calculated using CCDC's Mercury or IUCr's checkCIF tools after manual removal of the solvent molecule atoms, reveals several trends in the porosity of halogen-bonded ionic cocrystals (Table 2). As expected, solvent inclusion plays a dominant role in expanding accessible volume, with solvated ionic cocrystals exhibiting significantly higher helium-accessible volumes and maximum pore diameters than their solvent-free analogues. The identity of the halogen also influences porosity: iodine-based systems consistently show larger voids and wider pores than their bromine- or chlorine-containing counterparts, likely due to iodine's greater polarizability, larger size, and stronger, more directional halogen bonding (Fig. 5 and 6).

Higher donor-to-acceptor stoichiometries (*e.g.*,  $4:4$  or  $3:3$ ) further enhance porosity, especially when paired with solvent inclusion, promoting the formation of more open and stable supramolecular frameworks. Unsurprisingly, a strong correlation is observed between maximum pore diameter and solvent-accessible void volume, though exceptions—such as the  $4(\text{NMe}_3\text{BzI}):4(p\text{-F}_4\text{DIB}):3(\text{Ac})$  ionic cocrystal—highlight the limitations of automated void analysis. A significant jump in void volumes is observed between the solvated and unsolvated architectures, with approximately a 35% increase in maximum pore diameter between  $4(\text{NMe}_3\text{BzI}):5(p\text{-F}_4\text{DIB})$ , which has the largest pore diameter among the unsolvated

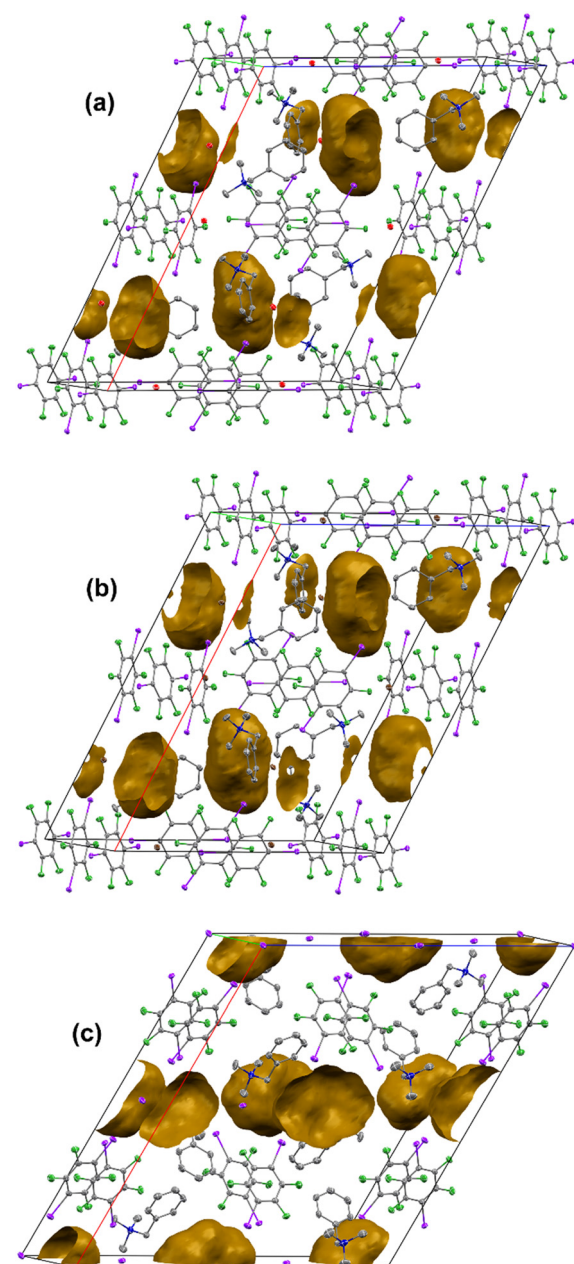


Fig. 5 Solvent voids in  $2(\text{NMe}_3\text{BzCl}):2(p\text{-F}_4\text{DIB}):MeCN$  (a),  $2(\text{NMe}_3\text{BzBr}):2(p\text{-F}_4\text{DIB}):MeCN$  (b), and  $4(\text{NMe}_3\text{BzI}):4(p\text{-F}_4\text{DIB}):MeCN$  (c).



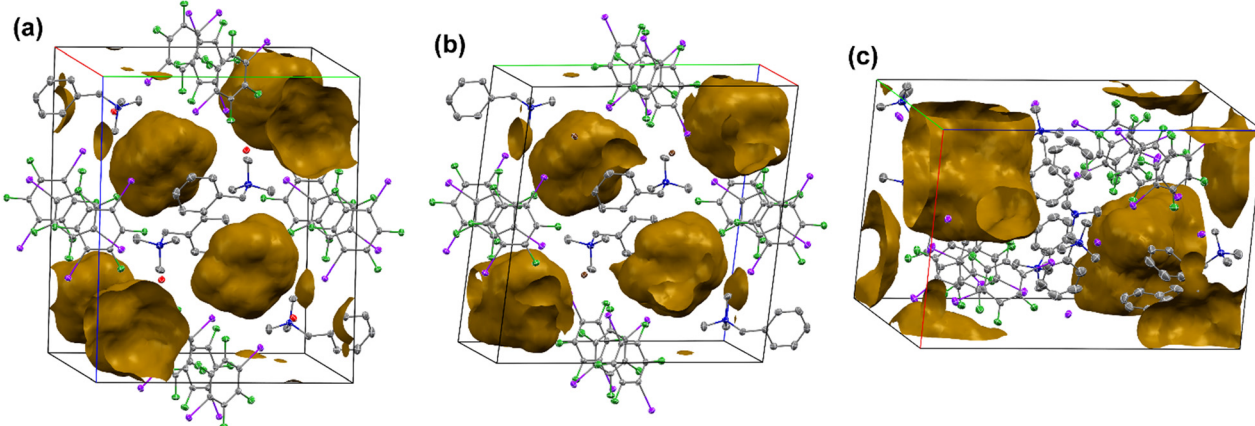


Fig. 6 Solvent voids in  $\text{NMe}_3\text{BzCl}$ : $p\text{-F}_4\text{DIB}$ : $\text{Ac}$  (a),  $\text{NMe}_3\text{BzBr}$ : $p\text{-F}_4\text{DIB}$ : $\text{Ac}$  (b), and  $4(\text{NMe}_3\text{BzI})$ : $4(p\text{-F}_4\text{DIB})$ : $3(\text{Ac})$  (c). The  $a$  axis is red, the  $b$  axis is green, and the  $c$  axis is blue.

structures, and  $4(\text{NMe}_3\text{BzI})$ : $4(p\text{-F}_4\text{DIB})$ : $\text{MeCN}$ , which has the smallest pore diameter of the solvated structures. The Kitagorodskii Packing Index (KPI), as calculated by the CALC VOID routine of PLATON, shows similar jumps. Within the

iodide salt-containing structures, there is a 5–10% decrease in the KPI when comparing solvated structures to their solvent-removed structures. Stable structures including the solvent contribution typically had KPI values of 65% of

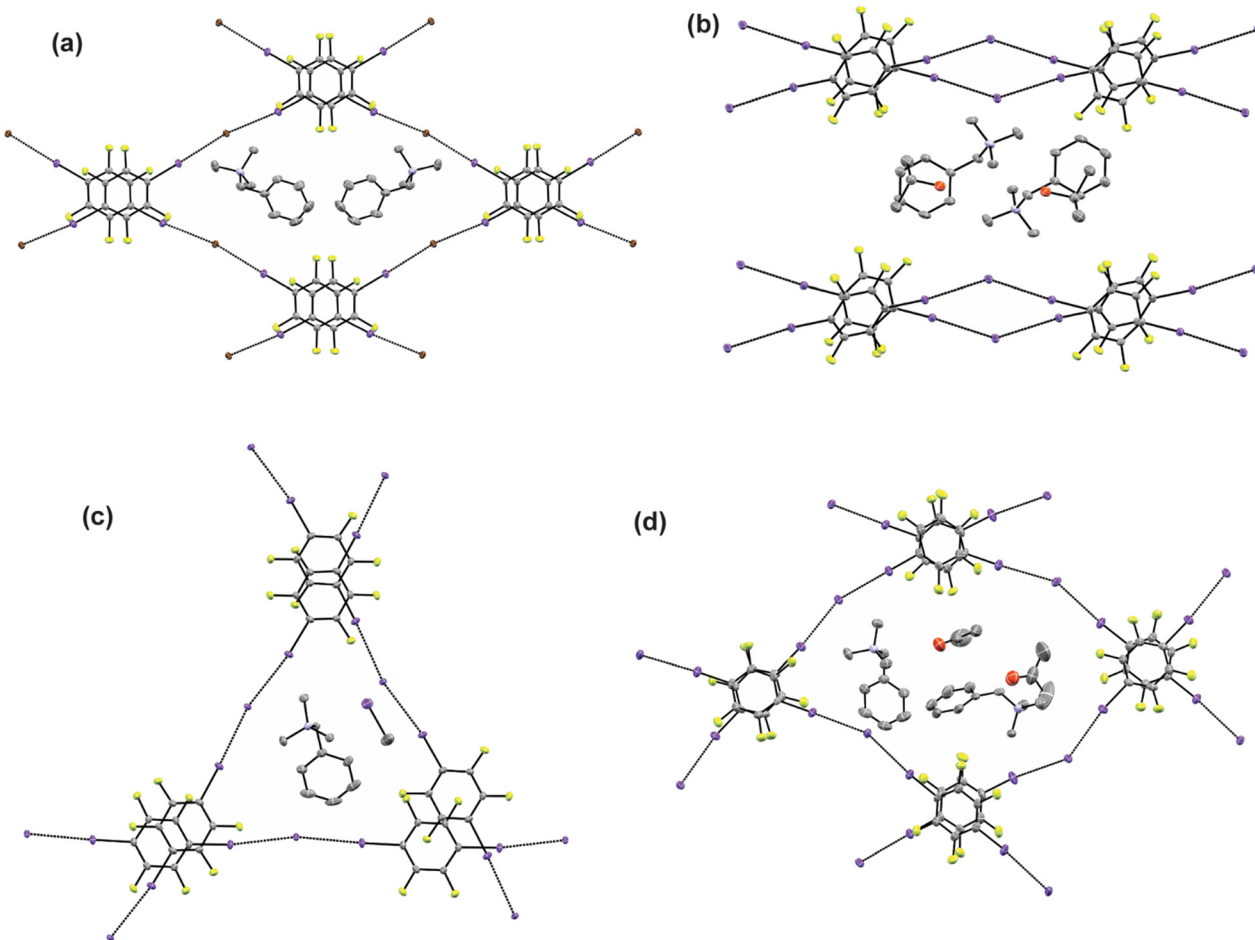


Fig. 7 Solvent and cation containing channels formed in  $\text{NMe}_3\text{BzBr}$ : $p\text{-F}_4\text{DIB}$  (a),  $\text{NMe}_3\text{BzI}$ : $p\text{-F}_4\text{DIB}$ : $i\text{-PrOH}$  (b),  $\text{NMe}_3\text{BzI}$ : $p\text{-F}_4\text{DIB}$ : $\text{CH}_3\text{I}$  (c), and  $4(\text{NMe}_3\text{BzI})$ : $4(p\text{-F}_4\text{DIB})$ : $3(\text{Ac})$  (d). Hydrogen atoms are omitted for clarity. Atomic displacement ellipsoids are displayed at the 50% probability level.

higher, whereas manually removing the solvent molecules and recalculating the KPI shows values between 57% and 65%. This compares favorably to the stable lattices formed by unsolvated ionic cocrystals, showing KPI values greater than 62%.

### Packing scope and limitations of 1:1 ionic cocrystals of $\text{NMe}_3\text{BzX}\text{-}p\text{-F}_4\text{DIB}$ and their solvates

It is apparent from the void analysis above that equimolar ionic cocrystal ratios of  $\text{NMe}_3\text{BzI}\text{-}p\text{-F}_4\text{DIB}$  adopt packing arrangements with significant void space that is ultimately occupied by solvent molecules. Given the variation in structure types observed in this series of structures (Table SI1) it seems the 1:1 iodide lattice is particularly flexible to accommodate the diversity of solvents studied here. Several packing themes were observed. In the 1:1 unsolvated systems  $\text{NMe}_3\text{BzCl}\text{-}p\text{-F}_4\text{DIB}$  and  $\text{NMe}_3\text{BzBr}\text{-}p\text{-F}_4\text{DIB}$  (Fig. 7a), a similar rhomboidal channel contained the ammonium component. A frequent arrangement obtained in the iodide-containing, solvated systems was the consolidation of the solvent and ammonium molecules between sheets of the halogen containing components, exemplified by  $\text{NMe}_3\text{BzI}\text{-}p\text{-F}_4\text{DIB}\text{-}i\text{-PrOH}$  (Fig. 7b). The ionic cocrystal obtained from iodomethane displays a trigonal channel (Fig. 7c). Finally, the ionic cocrystal obtained from acetone shows a more distorted rhomboidal channel hosting the solvent molecules and ammonium cations (Fig. 7d). In all cases, the alignment of chains also serves to localize the fluorinated portion of the structure throughout the lattice.

## Conclusions

The reaction of the common halogen bond donor 1,4-diiodotetrafluorobenzene (*p*-F<sub>4</sub>DIB) with the halide salts of the trimethylbenzyl ammonium cation ( $\text{NMe}_3\text{BzX}$ , X = Cl, Br, I) in a wide variety of organic solvents revealed a strong correlation between the identity of the halide anion and the resulting solid-state structure. When utilizing  $\text{NMe}_3\text{BzI}$ , a strong preference for solvated structures was observed, with eight solvated and three unsolvated motifs observed across 11 solvents. The unsolvated structures were obtained with the unequal  $\text{NMe}_3\text{BzI}$  to *p*-F<sub>4</sub>DIB ratios 2:3, 8:3, and 4:5. In contrast, the solvated structures were all obtained in equal halogen bond acceptor:donor ratios, with  $\text{NMe}_3\text{BzI}\text{-}p\text{-F}_4\text{DIB}$ :solvent ratios of 1:1:1, 2:2:1, and 4:4:1. The preference for solvation in the solid state is reversed when moving to the  $\text{NMe}_3\text{BzBr}$  and  $\text{NMe}_3\text{BzCl}$  systems, with the majority of the structures obtained being free from solvent inclusion. Across seven solvents in the  $\text{NMe}_3\text{BzBr}$  system (excluding iodomethane), five unsolvated structures, in 1:1, 3:4, and 4:5 acceptor:donor ratios, and two solvated structures, in 1:1:1 and 2:2:1 acceptor:donor:solvent ratios, were obtained. When moving to  $\text{NMe}_3\text{BzCl}$ , the preference for unsolvated structures continues, with six different solvents providing the same 1:1  $\text{NMe}_3\text{BzCl}\text{-}p\text{-F}_4\text{DIB}$  structure. Three other solvated structures were obtained in 1:1:1, 2:2:2,

and 3:3:2 ratios. The crystal packing and halogen bonding motifs were identical, except for the slight size difference of the halogen anion, in bromide- and chloride-containing crystals of the same ratios. In the iodides we observe two instances where the ionic cocrystal ratio approaches 1:1 (in the 2:3 ionic cocrystal and the 4:5 ionic cocrystal) that form sufficiently condensed packing lattices without solvent incorporation. But in a true equimolar ratio of  $\text{NMe}_3\text{BzI}\text{-}p\text{-F}_4\text{DIB}$ , we have not yet observed packing that is entirely supported by solvent-free halogen bonding. These results highlight the versatility of halogen bonding to accommodate a variety of packing motifs, as well as its sensitivity to reaction conditions.

## Author contributions

The manuscript was written through the contributions of all authors. All authors have given approval to the final version of the manuscript.

## Conflicts of interest

There are no conflicts to declare.

## Data availability

Supplementary information (SI): For ESI and crystallographic data in CIF or other electronic format. See DOI: <https://doi.org/10.1039/d5ce00832h>.

CCDC 2477133–2477141, 2477245, 2477246 and 2477290–2477298 contain the supplementary crystallographic data for this paper.<sup>59a–t</sup>

## Acknowledgements

AJP acknowledges the United States Air Force Institute of Technology Civilian Institutions for fellowship support.

## References

- 1 G. Cavallo, P. Metrangolo, R. Milani, T. Pilati, A. Priimagi, G. Resnati and G. Terraneo, *Chem. Rev.*, 2016, **116**, 2478–2601.
- 2 G. R. Desiraju, P. Shing Ho, L. Kloo, A. C. Legon, R. Marquardt, P. Metrangolo, P. Politzer, G. Resnati and K. Rissanen, *Pure Appl. Chem.*, 2013, **85**, 1711–1713.
- 3 N. Baus Topić, N. Bedeković, K. Lisac, V. Stilinović and D. Činčić, *Cryst. Growth Des.*, 2022, **22**, 3981–3989.
- 4 L. H. E. Wieske and M. Erdélyi, *J. Am. Chem. Soc.*, 2024, **146**, 3–18.
- 5 M. Erdélyi, C. Esterhuyse and W. Zhu, *Chem.*, 2021, **86**, 1229–1230.
- 6 S. An, A. Hao and P. Xing, *ACS Nano*, 2022, **16**, 19220–19228.
- 7 B. Topaloğlu Aksoy, B. Dedeoglu, Y. Zorlu, M. M. Ayhan and B. Çoşut, *CrystEngComm*, 2022, **24**, 5630–5641.
- 8 E. Nieland, D. Komisarek, S. Hohloch, K. Wurst, V. Vasylyeva, O. Weingart and B. M. Schmidt, *Chem. Commun.*, 2022, **58**, 5233–5236.



9 P. Politzer, J. S. Murray and T. Clark, *Phys. Chem. Chem. Phys.*, 2013, **15**, 11178–11189.

10 L. C. Gilday, S. W. Robinson, T. A. Barendt, M. J. Langton, B. R. Mullaney and P. D. Beer, *Chem. Rev.*, 2015, **115**, 7118–7195.

11 D. M. Ivanov, N. A. Bokach, V. Yu. Kukushkin and A. Frontera, *Chem. – Eur. J.*, 2022, **28**, 1–12.

12 P. Metrangolo, F. Meyer, T. Pilati, G. Resnati and G. Terraneo, *Angew. Chem., Int. Ed.*, 2008, **47**, 6114–6127.

13 (a) P. Metrangolo, F. Meyer, T. Pilati, G. Resnati and G. Terraneo, *Chem. – Eur. J.*, 2001, **7**, 2511–2519.

14 J. Xu, X. Liu, T. Lin, J. Huang and C. He, *Macromolecules*, 2005, **38**, 3554–3557.

15 P. Metrangolo, C. Präsang, G. Resnati, R. Liantonio, A. C. Whitwood and D. W. Bruce, *Chem. Commun.*, 2006, 3290–3292.

16 J. Xu, X. Liu, J. K. P. Ng, T. Lin and C. He, *J. Mater. Chem.*, 2006, **16**, 3540–3545.

17 M. H. Kolář and O. Tabarrini, *J. Med. Chem.*, 2017, **60**, 8681–8690.

18 L. Mendez, G. Henriquez, S. Sirimulla and M. Narayan, *Molecules*, 2017, **22**, 1–15.

19 A. J. Cruz-Cabeza, S. Karki, L. Fábián, T. Frić, G. M. Day and W. Jones, *Chem. Commun.*, 2010, **46**, 2224–2226.

20 S. Cherukuvada and A. Nangia, *Chem. Commun.*, 2014, **50**, 906–923.

21 A. M. Healy, Z. A. Worku, D. Kumar and A. M. Madi, *Adv. Drug Delivery Rev.*, 2017, **117**, 25–46.

22 S. J. Dalgarno, P. K. Thallapally, J. Tian and J. L. Atwood, *New J. Chem.*, 2008, **32**, 2095–2099.

23 D. Giron, *J. Therm. Anal. Calorim.*, 2001, 37–60.

24 A. Nangia, *Cryst. Growth Des.*, 2006, **6**, 2–4.

25 D. Braga, F. Grepioni, L. Maini and M. Polito, in *Molecular Networks (Structure and Bonding)*, ed. M. W. Hosseini, Springer, 2009, vol. 132, pp. 25–50.

26 G. P. Stahly, *Cryst. Growth Des.*, 2007, **7**, 1007–1026.

27 L. Turunen, F. Pan, N. K. Beyeh, M. Cetina, J. F. Trant, R. H. A. Ras and K. Rissanen, *CrystEngComm*, 2017, **19**, 5223–5229.

28 Y. Vasilopoulos, J. Heyda, J. Rohlíček, E. Skořepová, V. Zvoníček and M. Šooš, *J. Phys. Chem. B*, 2022, **126**, 503–512.

29 A. Mukherjee, S. Tothadi and G. R. Desiraju, *Acc. Chem. Res.*, 2014, **47**, 2514–2524.

30 H. T. Le and A. Goto, *Cell Rep. Phys. Sci.*, 2021, **2**, 1–21.

31 N. B. Topić, E. Topić, L. Fotović and V. Stilinović, *Cryst. Growth Des.*, 2024, **24**, 1214–1226.

32 L. Posavec, V. Nemec, V. Stilinović and D. Cinčić, *Cryst. Growth Des.*, 2021, **21**, 6044–6050.

33 C. Loy, M. Zeller and S. V. Rosokha, *Crystals*, 2020, **10**, 1–14.

34 P. V. Petunin, E. V. Tretyakov, M. K. Shurikov, D. E. Votkina, G. V. Romanenko, A. A. Dmitriev, N. P. Gritsan, D. M. Ivanov, R. M. Gomila, A. Frontera, G. Resnati, V. Y. Kukushkin and P. S. Postnikov, *Cryst. Growth Des.*, 2024, **24**, 2104–2116.

35 R. Liu, H. Wang and W. J. Jin, *Cryst. Growth Des.*, 2017, **17**, 3331–3337.

36 J. M. Rautiainen, A. Valkonen, J. Lundell, K. Rissanen and R. Puttreddy, *Adv. Sci.*, 2024, **11**, 1–12.

37 K. Lisac and D. Cinčić, *Crystals*, 2017, **7**, 1–11.

38 K. Raatikainen and K. Rissanen, *Cryst. Growth Des.*, 2010, **10**, 3638–3646.

39 K. Kobra, S. O'Donnell, A. Ferrari, C. D. McMillen and W. T. Pennington, *New J. Chem.*, 2018, **42**, 10518–10528.

40 M. C. Pfrunder, A. S. Micallef, L. Rintoul, D. P. Arnold, K. J. P. Davy and J. McMurtrie, *Cryst. Growth Des.*, 2014, **14**, 6041–6047.

41 J. Viger-Gravel, I. Korobkov and D. L. Bryce, *Cryst. Growth Des.*, 2011, **11**, 4984–4995.

42 A. S. Mikherdov, M. Jin and H. Ito, *Chem. Sci.*, 2023, **14**, 4485–4494.

43 X. Ding, M. Tuikka and M. Haukka, *Crystals*, 2020, **10**, 1–12.

44 L. Posavec and D. Cinčić, *Cryst. Growth Des.*, 2024, **24**, 7514–7523.

45 Y. N. Toikka, G. L. Starova, V. V. Suslonov, R. M. Gomila, A. Frontera, V. Y. Kukushkin and N. A. Bokach, *Cryst. Growth Des.*, 2023, **23**, 5194–5203.

46 H. M. Tang, Z. Y. Quan, B. Ding, X. G. Wang, B. Tang, Z. G. Huang and E. C. Yang, *Cryst. Growth Des.*, 2024, **24**, 5211–5221.

47 L. Happonen, J. M. Rautiainen and A. Valkonen, *Cryst. Growth Des.*, 2021, **21**, 3409–3419.

48 S. Shankar, O. Chovnik, L. J. W. Shimon, M. Lahav and M. E. Van Der Boom, *Cryst. Growth Des.*, 2018, **18**, 1967–1977.

49 C. F. MacRae, I. Sovago, S. J. Cottrell, P. T. A. Galek, P. McCabe, E. Pidcock, M. Platings, G. P. Shields, J. S. Stevens, M. Towler and P. A. Wood, *J. Appl. Crystallogr.*, 2020, **53**, 226–235.

50 A. L. Spek, *Inorg. Chim. Acta*, 2018, **470**, 232–237.

51 A. L. Spek, *J. Appl. Crystallogr.*, 2003, **36**, 7–13.

52 A. L. Spek, *Acta Crystallogr., Sect. D: Biol. Crystallogr.*, 2009, **65**, 148–155.

53 Bruker, *Bruker AXS*, 2017.

54 G. M. Sheldrick, *Acta Crystallogr., Sect. C: Struct. Chem.*, 2015, **71**, 3–8.

55 O. V. Dolomanov, L. J. Bourhis, R. J. Gildea, J. A. K. Howard and H. Puschmann, *J. Appl. Crystallogr.*, 2009, **42**, 339–341.

56 A. L. Spek, *J. Appl. Crystallogr.*, 2003, **36**, 7–13.

57 L. Brammer, E. A. Bruton and P. Sherwood, *Cryst. Growth Des.*, 2001, **1**, 277–290.

58 J. P. M. Lommerse, A. J. Stone, R. Taylor and F. H. Allen, *J. Am. Chem. Soc.*, 1996, **118**, 3108–3116.

59 (a) CCDC 2477133: Experimental Crystal Structure Determination, 2025, DOI: [10.5517/ccdc.csd.cc2p4nj1](https://doi.org/10.5517/ccdc.csd.cc2p4nj1); (b) CCDC 2477134: Experimental Crystal Structure Determination, 2025, DOI: [10.5517/ccdc.csd.cc2p4nk2](https://doi.org/10.5517/ccdc.csd.cc2p4nk2); (c) CCDC 2477135: Experimental Crystal Structure Determination, 2025, DOI: [10.5517/ccdc.csd.cc2p4nl3](https://doi.org/10.5517/ccdc.csd.cc2p4nl3); (d) CCDC 2477136: Experimental Crystal Structure Determination, 2025, DOI: [10.5517/ccdc.csd.cc2p4nm4](https://doi.org/10.5517/ccdc.csd.cc2p4nm4); (e) CCDC 2477137: Experimental Crystal Structure Determination, 2025, DOI: [10.5517/ccdc.csd.cc2p4nn5](https://doi.org/10.5517/ccdc.csd.cc2p4nn5); (f)



CCDC 2477138: Experimental Crystal Structure Determination, 2025, DOI: [10.5517/ccdc.csd.cc2p4np6](https://doi.org/10.5517/ccdc.csd.cc2p4np6); (g)  
 CCDC 2477139: Experimental Crystal Structure Determination, 2025, DOI: [10.5517/ccdc.csd.cc2p4nq7](https://doi.org/10.5517/ccdc.csd.cc2p4nq7); (h)  
 CCDC 2477140: Experimental Crystal Structure Determination, 2025, DOI: [10.5517/ccdc.csd.cc2p4nr8](https://doi.org/10.5517/ccdc.csd.cc2p4nr8); (i)  
 CCDC 2477141: Experimental Crystal Structure Determination, 2025, DOI: [10.5517/ccdc.csd.cc2p4ns9](https://doi.org/10.5517/ccdc.csd.cc2p4ns9); (j)  
 CCDC 2477245: Experimental Crystal Structure Determination, 2025, DOI: [10.5517/ccdc.csd.cc2p4s4s](https://doi.org/10.5517/ccdc.csd.cc2p4s4s); (k)  
 CCDC 2477246: Experimental Crystal Structure Determination, 2025, DOI: [10.5517/ccdc.csd.cc2p4s5t](https://doi.org/10.5517/ccdc.csd.cc2p4s5t); (l)  
 CCDC 2477290: Experimental Crystal Structure Determination, 2025, DOI: [10.5517/ccdc.csd.cc2p4tl8](https://doi.org/10.5517/ccdc.csd.cc2p4tl8); (m)  
 CCDC 2477291: Experimental Crystal Structure

Determination, 2025, DOI: [10.5517/ccdc.csd.cc2p4tm9](https://doi.org/10.5517/ccdc.csd.cc2p4tm9); (n)  
 CCDC 2477292: Experimental Crystal Structure Determination, 2025, DOI: [10.5517/ccdc.csd.cc2p4tnb](https://doi.org/10.5517/ccdc.csd.cc2p4tnb); (o)  
 CCDC 2477293: Experimental Crystal Structure Determination, 2025, DOI: [10.5517/ccdc.csd.cc2p4tpc](https://doi.org/10.5517/ccdc.csd.cc2p4tpc); (p)  
 CCDC 2477294: Experimental Crystal Structure Determination, 2025, DOI: [10.5517/ccdc.csd.cc2p4tqd](https://doi.org/10.5517/ccdc.csd.cc2p4tqd); (q)  
 CCDC 2477295: Experimental Crystal Structure Determination, 2025, DOI: [10.5517/ccdc.csd.cc2p4trf](https://doi.org/10.5517/ccdc.csd.cc2p4trf); (r)  
 CCDC 2477296: Experimental Crystal Structure Determination, 2025, DOI: [10.5517/ccdc.csd.cc2p4tsg](https://doi.org/10.5517/ccdc.csd.cc2p4tsg); (s)  
 CCDC 2477297: Experimental Crystal Structure Determination, 2025, DOI: [10.5517/ccdc.csd.cc2p4tth](https://doi.org/10.5517/ccdc.csd.cc2p4tth); (t)  
 CCDC 2477298: Experimental Crystal Structure Determination, 2025, DOI: [10.5517/ccdc.csd.cc2p4tvj](https://doi.org/10.5517/ccdc.csd.cc2p4tvj).

